Pillared elastic metasurface with constructive interference for flexural wave manipulation

Liyun Cao, Zhichun Yang, Yanlong Xu, Zhaolin Chen, Yifan Zhu, Shiwang Fan, Krupali Donda, Brice Vincent, B. Assouar

Pillared Elastic Metasurface with Constructive Interference for Flexural Wave Manipulation steering

Liyun Cao[1,2], Zhichun Yang[1,*], Yanlong Xu[1], Zhaolin Chen[1],Yifan Zhu[2], Shiwang Fan[2], Krupali Donda[2], Brice Vincent[2] and Badreddine Assouar[2,*]

[1]*School of Aeronautics, Northwestern Polytechnical University, Xi'an, 710072, China*

[2]*Institut Jean Lamour, CNRS, Universite de Lorraine, Nancy, 54506, France*

*Corresponding author e-mails: yangzc@nwpu.edu.cn & badreddine.assouar@univ-lorraine.fr

Highlights

• A new conceptual design of pillared elastic metasurface (~0.495λ) with constructive interference (PEMC) is proposed to manipulate flexural waves.

• We systematically reveal the phase shift of transmitted waves across the improved subunits and establish an analytical model for multi-resonator subunits to accurately predict the phase shift and amplitude of the transmitted wave.

• The intrinsic physical of the constructive and destructive interferences through out-of-plane vibration of the plate for the two adjacent subunits are analyzed.

• Finally, we experimentally verify deflecting and focusing functionality of the proposed PEMC without any drilling or grooving the original plate surface.

Abstract

In engineering, plate structures are one type of the main load-bearing structures. However, most of designed plate-like metamaterials/metasurfaces need to be heavily grooved or drilled on the original plate surface, which will inevitably cause some

destruction to the strength and stiffness of the host plate structures. To overcome this weakness, we propose a new conceptual design of pillared elastic metasurface (~0.495λ) to manipulate flexural waves in plates by considering constructive interference. The interference, which manifests itself as the coupling through out-of-plane vibration of the plate for the two adjacent subunits, is analyzed to reveal the physical mechanisms. In addition, we reveal the mechanism of the phase shift of transmitted waves across the sub-wavelength subunits and establish an analytical model for the multi-resonator subunits to accurately predict the phase shift and amplitude of the transmitted wave. We theoretically design and experimentally demonstrate the deflecting and focusing functionalities of the proposed elastic metasurface. Our design can provide a new route to broad applications of the constructive interference in elastic metamaterials/metasurfaces, which can be used to efficiently engineer arbitrary wave profiles.

Keywords: Elastic metasurfaces, Constructive interference, Flexural waves, Metamaterials, Elastic waves

1. Introduction

Metasurface is one kind of ultrathin metamaterials, with a more compact and easily fabricated form. It has been recently proposed to realize extreme features of bulky metamaterials [1-8]. The studies on the metasurfaces with phase gradients, based on the generalized Snell's law (GSL) [9], have made a significant progress in the fields of optics [9-11] and acoustics [12-15]. Recently, the development of elastic metasurfaces, with complex inherent properties of different elastic wave types and mode conversions, has also attracted wide attentions of researchers.

The existing elastic metasurfaces can be classified into body wave metasurfaces [16-20], surface wave metasurfaces [21], and plate wave metasurfaces [22-33], according to the manipulated wave type. Among them, the plate wave metasurface is a hot one due to the universality of plate waves in engineering. For the first time, the concept of the optic metasurface or acoustic metasurface was extended to elastic wave metasurface in the field of solid mechanics by Zhu and Semperlotti [22]. They investigated the anomalous refraction of Lamb waves (plate waves in a relatively thick plate [34]) based on mode conversion by using geometric tapers. Meanwhile, Liu et al. [23] designed a zigzag structure metasurface by grooving the plate to achieve a source illusion device for flexural waves (plate waves in a relatively thin plate [34]). In order to further improve transmittance, a high transmission metasurface for deflecting and focusing in-plane longitudinal waves in a plate [24] was proposed by breaking the intrinsic proportional density-stiffness relation. Furthermore, in one [33] of our previous works, phase accumulation of the multi-resonators was used to experimentally

design and demonstrate the pillared metasurface, which is capable of deflecting vertically and obliquely incident flexural waves with high transmissions.

On the other hand, some tunable plate wave metasurfaces [35-38] were also proposed. An adaptive metasurface [35] capable of modulating A_0 Lamb waves in a plate were designed through the piezoelectric units. Furthermore, a programmable plate wave metasurface [36] with sensing-and-actuating units was introduced to adapt and reprogram flexural wave control functionalities in real time. Recently, a switchable multifunctional fish-bone elastic metasurface [37] is proposed to manipulate the transmitted plate waves. More recently, plate wave metasurfaces had been applied to total mode conversions from in-plane longitudinal waves to shear waves [39], splitting flexural waves [40], asymmetrical flexural wave transmission [41] and isolating vibration [42].

Almost all of the above mentioned elastic metasurfaces need to be grooved on the complete plate surface, which avoids the coupling interference (CI) between two adjacent subunits to design them independently. The CI is similar to the Fano interference [43-46], which results from the coupling between individual unit-scatters in the continuum background, i.e., the host plate. However, the CI in our work pays more attention to the coupling of the adjacent subunits deviating from the resonance frequency.

In the present research, we improve the model reported in our previous paper [33] by the iron pillared-resonator subunits. The lowest dispersion band and vibration mode analyses are used to explain the working mechanism of the phase shift of transmitted

waves. Furthermore, we indeed propose an analytical model for multi-pillared subunit to accurately predict the amplitude and phase shift of the transmitted wave. Based on the improved subunit model, the physical mechanisms of CI between the adjacent subunits are revealed, which can be classified into the constructive and destructive interferences. Further, by considering the CI, we propose the pillared elastic metasurface with constructive interference (PEMC) to manipulate flexural waves propagating in a plate. Finally, experimental validations are carried out to demonstrate the deflecting and focusing capabilities of the designed PEMCs.

2. Theoretical design of the subunit of PEMC

Fig. 1(a) depicts the PEMC structure (enlarged one is shown in the top of the figure) without slots. To clarify the difference between the current work and our previous one [33], the sketches of the previous elastic metasurface with slots and the present one without slots in a front view (*xy*-plane) are shown in Figs. 1(d) and 1(e), respectively. The most obvious difference is that CI will exist at the junction of the adjacent subunits for the metasurface without slots (marked in Fig. 1(e)). The interference manifests itself as the coupling through out-of-plane vibration of the plate for the two adjacent subunits. In addition, the previous subunits are improved by the iron pillared-resonator subunits. Considering the CI, the present elastic metasurface is composed of the improved three-dimensional (3D) subunits, periodically arrayed on the host plate, as shown in Fig. 1(b). The subunit design is one of the core design components. For simplicity, we firstly design the corresponding two-dimensional (2D) subunits, which is the cross-section view, as shown in Fig. 1(c). Then, it will be expanded to the 3D one.

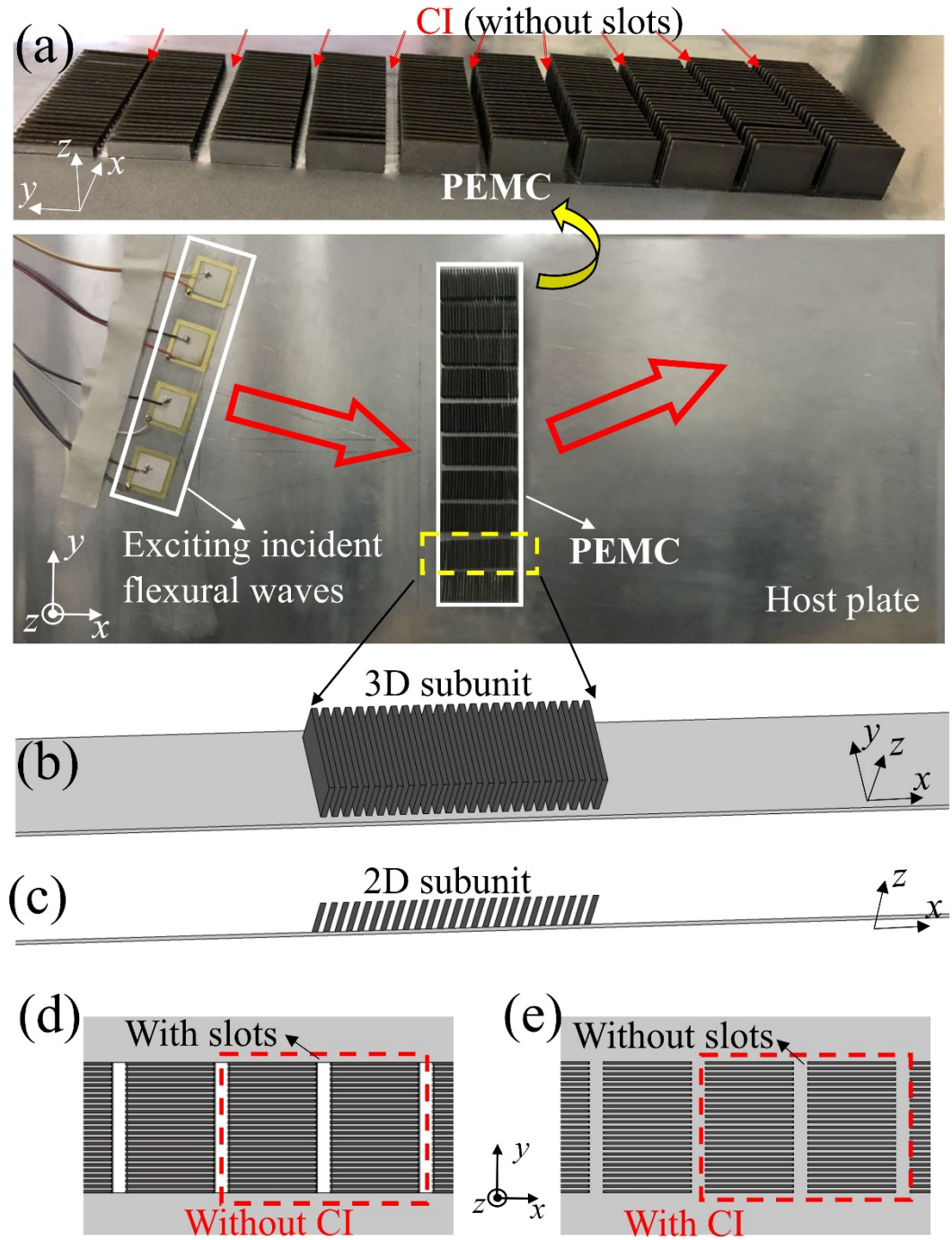

Fig. 1. (a) Sketch of the PEMC capable of deflecting an incident flexural wave, with the enlarged view in the top. (b) illustrates the three-dimensional (3D) subunit corresponding to the dotted box in (a). (c) The corresponding two-dimensional (2D) subunit, which is the cross-section view of the 3D one. (d) and (e) illustrate the adjacent subunits without CI and with CI in a front view (*xy*-plane), respectively.

2.1. Mechanism of phase shift in the multi-resonator subunit

The 2D subunit is based on the pillared resonators periodically arrayed and bonded on the surface of a thin aluminum alloy plate, as shown in Fig. 1(c). Here, two types of pillared resonators are analyzed, which are made of aluminum alloy (with the elastic modulus of $E_{\text{alu}} = 70$ GPa, Poisson's ratio of $\nu_{\text{alu}} = 0.33$, and the density of $\rho_{\text{alu}} = 2700$ kg/m^3) and iron (with the elastic modulus of $E_{\text{iro}} = 200$ GPa, Poisson's ratio of $\nu_{\text{iro}} = 0.29$, and the density of $\rho_{\text{iro}} = 7870$ kg/m^3). The elementary unit cells are illustrated in Figs. 2(a) and 2(b), where the black and grey areas represent the iron and aluminum alloy, respectively. Both of the plate and pillar thicknesses are *d*=1 mm. *D* denotes the constant lattice with 2 mm, and *h* is the pillar height. The periodicity is along the *x*-axis. Figs. 2(a) and 2(b) show the lowest dispersion bands (corresponding to flexural waves in the plates) for different heights of the pillared resonators. They are obtained by using the eigen frequency analysis of COMSOL MULTIPHYSICS 5.4 software.

It can be observed from Figs. 2(a) and 2(b) that the wavenumbers *k* corresponding to the color lines (representing the plate with pillared resonators) are bigger than that corresponding to the black lines (representing the plate without resonators) at the same frequency. Furthermore, the wavenumber in the plate increases with the pillar height. According to $v = 2\pi f / k$, the wavenumber is inversely proportional to the corresponding wave velocity. Therefore, the wave velocity of the flexural wave propagating in the plate with the periodic structures decreases when the height of pillared resonator increase. After propagating the same distance, the flexural wave

with lower velocity will have a larger phase shift. Except for the above same characteristics, the difference between Figs. 2(a) and 2(b) is that the wavenumber of the flexural wave in the plate with periodic iron pillared resonators is larger than that in the plate with periodic aluminum alloy pillared resonators at the same frequency. It indicates that periodic iron resonators are easier to make the flexural waves in the plate slow down, i.e., phase shift. Therefore, the iron pillared resonator is adopted to improve the subunits in our previous paper [33].

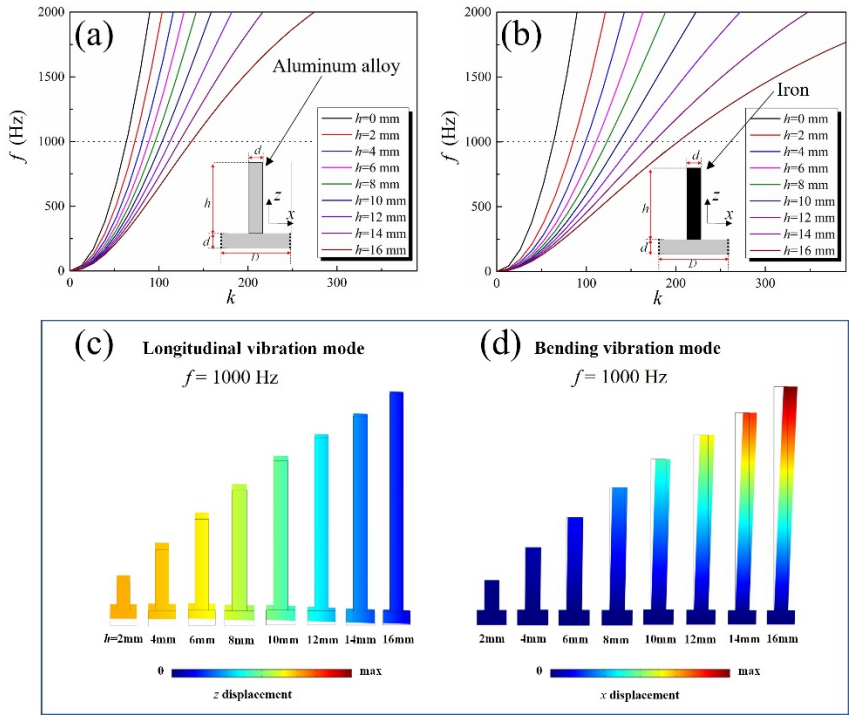

Fig. 2. (a) and (b) show the lowest dispersion bands for different heights of the aluminum alloy and iron pillared resonators, respectively. (c) and (d) illustrate the longitudinal and bending vibration modes of the iron pillared resonator with varying of the pillar height, respectively.

The targeted frequency in our design is 1 kHz, which is one of the typical low frequencies. In order to further reveal the interaction between the pillared resonators and flexural waves in the plate, the corresponding vibration modes of the iron resonator

are analyzed. Figs. 2(c) and 2(d) show the z direction displacements in the pillared resonators associated with longitudinal vibration modes (longitudinal waves) and the x direction displacements in the pillared resonators associated with bending vibration modes (flexural waves), respectively. It can be found that when the pillar height is short (less than 6d), the longitudinal vibration of the pillared resonator (the longitudinal wave) is dominant, while when the pillar height is high (more than 14d), the bending vibration (the flexural wave) is dominant. From this propagation form in the resonators, it makes one easy to understand the dispersion bands in Figs. 2(a) and 2(b). When the propagating flexural waves in the plate encounter a resonator, parts of them are converted into longitudinal waves or flexural waves in the resonator, which will propagate in the resonator and then to the plate. This transmission process leads to slow flexural waves down to have a big phase shift. In this way, the wave velocity of the longitudinal wave or the flexural wave in the iron pillared resonator is lower than the one in the aluminum alloy resonator. In other words, the transmission speed in the iron resonator is slower than the one in the aluminum alloy resonator. The transmission process with the slower speed will lead to a larger phase shit. Then, we can easily understand that the improved subunits based on periodic iron resonators are easier to make the flexural waves phase shit.

2.2. Analytical transmission and phase spectra of the 2D subunit

In the current study, the number of pillared resonators is set as 25. It makes multi-resonators structure approximate the above mentioned infinite periodic subunits to compose the subunits, as shown in Fig. 3(a), which will cause the phase shifts of

transmitted flexural waves in a plate. The working mechanism of the phase shifts of transmitted flexural waves across the subunits has been revealed by the above lowest dispersion band and vibration mode analysis. The subunits with different pillar heights make it possible to meet the desired phase profile for designing a gradient metasurface. In addition, the evenly distributed amplitude of transmitted waves across the subunits is also crucial in designing a metasurface without any undesired distortion for transmitted pattern [24, 33]. Therefore, both amplitudes and phase shifts of transmitted waves across the subunits need to be accurately solve.

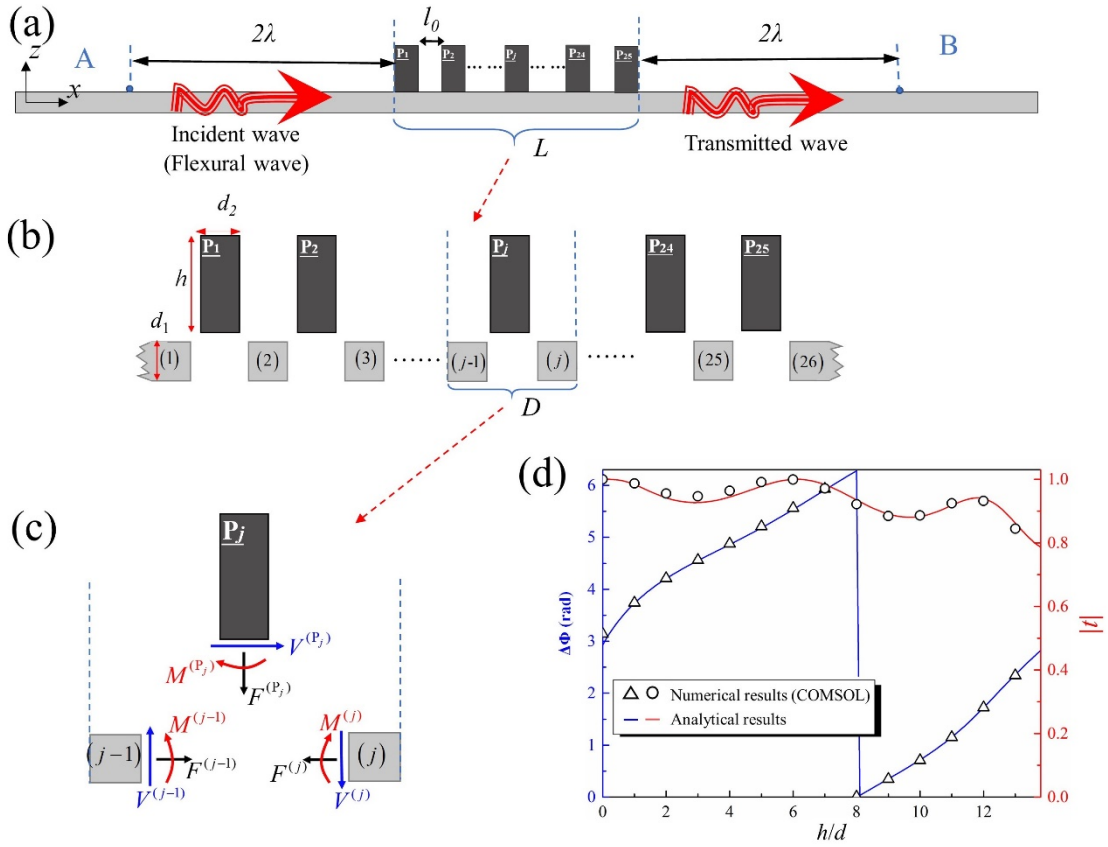

Fig. 3. (a) Sketch of the 2D subunit with 25 pillared resonators. The host plate is divided into several regions, which are marked as the 1st, 2nd, …, 26th regions in (b). (c) illustrates the (j-1)th region, jth region, and jth pillared resonator. (d) shows the analytical and simulated results of the phase shift and amplitude for the transmitted waves by varying the pillar height.

To solve amplitudes and phase shifts of the transmitted waves, we establish the analytical model and divide the host plate into several regions, which are marked as the 1st, 2nd, …, 26th regions, respectively, in Fig. 3(b). First, wave transmission in the (j-1)th region, j^{th} region, and j^{th} pillared resonator are studied, as shown in Fig. 3(c). From the above analysis of Figs. 2(c) and 2(d), we know that both flexural waves (bending vibrations) and longitudinal waves (longitudinal vibrations) will couple and exist in the pillared resonator. Therefore, for accuracy, they must be considered in the pillared resonator and host plate at the same time. It should be pointed out that flexural and longitudinal waves are equivalent to A0 and S0 lamb waves, respectively, in the low designed frequency of 1 kHz [34]. The governing equations for flexural waves and longitudinal waves in the host plate can be expressed in the following forms, respectively:

$$\begin{aligned} E_1 I_1 \frac{\partial^4 w(x,t)}{\partial x^4} + \rho_1 d_1 \frac{\partial^2 w(x,t)}{\partial t^2} = 0 \\ \frac{E_1}{(1-\nu_1^2)} \frac{\partial^2 u(x,t)}{\partial x^2} - \rho_1 \frac{\partial^2 u(x,t)}{\partial t^2} = 0 \end{aligned}, \quad (1)$$

where E_1, ρ_1, and I_1 are the Young's modulus, density, and section moment of inertia of the plate, respectively. $I_1 = \frac{d_1^3}{12(1-\nu_1^2)}$, in which d_1 and ν_1 are the thickness of the plate and Poisson's ratio of the material, respectively. The general solutions of the displacements for the flexural wave equations in the (j-1)th and j^{th} regions are:

$$w^{(j-1)}(x,t)=\left(A^{(j-1)}e^{-ik_{b1}x}+B^{(j-1)}e^{ik_{b1}x}+C^{(j-1)}e^{-k_{b1}x}+D^{(j-1)}e^{k_{b1}x}\right)e^{i\omega t}$$
$$w^{(j)}(x,t)=\left(A^{(j)}e^{-ik_{b1}x}+B^{(j)}e^{ik_{b1}x}+C^{(j)}e^{-k_{b1}x}+D^{(j)}e^{k_{b1}x}\right)e^{i\omega t} \quad (2)$$

where the superscripts (j-1) and (j) indicate the (j-1)$^{\text{th}}$ and j^{th} regions, respectively. The flexural wavenumber is $k_{b1}=\left(\frac{\rho_1 d_1\omega^2}{E_1 I_1}\right)^{1/4}$, in which $\omega=2\pi f$ is the circular frequency. $A^{(j\text{-}1)}$, $B^{(j\text{-}1)}$, $C^{(j\text{-}1)}$, $D^{(j\text{-}1)}$, $A^{(j)}$, $B^{(j)}$, $C^{(j)}$, and $D^{(j)}$ are complex coefficients. $A^{(j\text{-}1)}e^{-ik_{b1}x}$ and $A^{(j)}e^{-ik_{b1}x}$ correspond to the positive-going propagating flexural waves, whereas $B^{(j\text{-}1)}e^{ik_{b1}x}$ and $B^{(j)}e^{ik_{b1}x}$ correspond to the negative-going propagating flexural waves. $C^{(j\text{-}1)}e^{-k_{b1}x}$ and $C^{(j)}e^{-k_{b1}x}$ correspond to the positive-going evanescent flexural waves, whereas $D^{(j\text{-}1)}e^{k_{b1}x}$ and $D^{(j)}e^{k_{b1}x}$ correspond to the negative-going evanescent flexural waves. The general solutions of the displacements for longitudinal wave equations in the (j-1)$^{\text{th}}$ and j^{th} regions are:

$$u^{(j-1)}(x,t)=\left(P^{(j\text{-}1)}e^{-ik_{l1}x}+Q^{(j\text{-}1)}e^{ik_{l1}x}\right)e^{i\omega t}$$
$$u^{(j)}(x,t)=\left(P^{(j)}e^{-ik_{l1}x}+Q^{(j)}e^{ik_{l1}x}\right)e^{i\omega t} \quad (3)$$

where the longitudinal wavenumber is $k_{l1}=\left[\frac{\rho_1\omega^2(1-\nu_1^2)}{E_1}\right]^{1/2}$, $P^{(j\text{-}1)}$, $Q^{(j\text{-}1)}$, $P^{(j)}$, and $Q^{(j)}$ are complex coefficients. $P^{(j\text{-}1)}e^{-ik_{l1}x}$ and $P^{(j)}e^{-ik_{l1}x}$ correspond to the positive-going propagating longitudinal waves, whereas $Q^{(j\text{-}1)}e^{ik_{l1}x}$ and $Q^{(j)}e^{ik_{l1}x}$ correspond to the negative-going propagating longitudinal waves.

The governing equations for the flexural wave and longitudinal wave in the pillared resonator j can be expressed in the following forms, respectively:

$$E_2 I_2 \frac{\partial^4 w(z,t)}{\partial z^4} + \rho_2 d_2 \frac{\partial^2 w(z,t)}{\partial t^2} = 0$$

$$\frac{E_2}{(1-\nu_2^2)} \frac{\partial^2 u(z,t)}{\partial z^2} - \rho_2 \frac{\partial^2 u(z,t)}{\partial t^2} = 0 \quad , \tag{4}$$

where E_2, ρ_2, and I_2 are the Young's modulus, density, and section moment of inertia of the pillared resonator, respectively. $I_2 = \frac{d_2^3}{12(1-\nu_2^2)}$, in which d_2 and ν_2 are the thickness of the resonator and Poisson's ratio of the material, respectively. The general solutions of the displacements for flexural wave and longitudinal wave equations in the j^{th} pillared resonator are

$$w^{(\mathrm{P}_j)}(z,t) = \left(A^{(\mathrm{P}_j)} e^{-ik_{b2}z} + B^{(\mathrm{P}_j)} e^{ik_{b2}z} + C^{(\mathrm{P}_j)} e^{-k_{b2}z} + D^{(\mathrm{P}_j)} e^{k_{b2}z} \right) e^{i\omega t}$$

$$u^{(\mathrm{P}_j)}(z,t) = \left(P^{(\mathrm{P}_j)} e^{-ik_{l2}z} + Q^{(\mathrm{P}_j)} e^{ik_{l2}z} \right) e^{i\omega t} \quad , \tag{5}$$

where the superscript (P_j) indicates the j^{th} pillared resonator. The flexural and longitudinal wavenumbers are $k_{b2} = \left(\frac{\rho_2 d_2 \omega^2}{E_2 I_2} \right)^{1/4}$ and $k_{l2} = \left[\frac{\rho_2 \omega^2 (1-\nu_2^2)}{E_2} \right]^{1/2}$, respectively. $A^{(\mathrm{P}_j)}$, $B^{(\mathrm{P}_j)}$, $C^{(\mathrm{P}_j)}$, $D^{(\mathrm{P}_j)}$, $P^{(\mathrm{P}_j)}$ and $Q^{(\mathrm{P}_j)}$ are complex coefficients. $A^{(\mathrm{P}_j)} e^{-ik_{b2}z}$ and $B^{(\mathrm{P}_j)} e^{ik_{b2}z}$ correspond to the up-going and down-going propagating flexural waves, respectively, whereas $C^{(\mathrm{P}_j)} e^{-k_{b2}z}$ and $D^{(\mathrm{P}_j)} e^{k_{b2}z}$ correspond to the up-going and down-going evanescent flexural waves, respectively. $P^{(\mathrm{P}_j)} e^{-ik_{l2}z}$ and $Q^{(\mathrm{P}_j)} e^{ik_{l2}z}$ correspond to the up-going and down-going propagating longitudinal waves, respectively.

The physical quantities $w^{(j)}$, $u^{(j)}$, $\varphi^{(j)}$, $F^{(j)}$, $V^{(j)}$, $M^{(j)}$ and the complex coefficients $A^{(j)}$, $B^{(j)}$, $C^{(j)}$, $D^{(j)}$, $P^{(j)}$, $Q^{(j)}$ for every region in the plate can be organized as a state vector and a coefficients vector, respectively:

$$\mathbf{v}^{(j)}=\left\{w^{(j)},u^{(j)},\varphi^{(j)},F^{(j)},V^{(j)},M^{(j)}\right\}^{\mathrm{T}}$$
$$\mathbf{k}^{(j)}=\left\{A^{(j)},B^{(j)},C^{(j)},D^{(j)},P^{(j)},Q^{(j)}\right\}^{T} \quad (6)$$

where φ, $F^{(j)}$, $V^{(j)}$, and $M^{(j)}$ are slope, axial force, shear force and bending moment, respectively. For simplicity, the origins of coordinates x and z are set at the interface among the (j-1)$^{\text{th}}$ region, j^{th} region, and j^{th} pillared resonator. Substituting Eqs. (2) and (3) into Eq. (A13), we obtain

$$\mathbf{v}^{(j)}=N_1\cdot\mathbf{k}^{(j)},\quad j=1,2\cdots 26, \quad (7)$$

where N_1 is the transformation matrix between the state vector and the coefficient vector. It is shown in Appendix A. Substituting Eqs. (2), (3), (5), and (A13) into the boundary conditions among the (j-1)$^{\text{th}}$ region, j^{th} region, and j^{th} pillared resonator (Eqs. (A1)-(A12)), we obtain

$$\begin{aligned}&N_2\left[A^{(j)},B^{(j)},C^{(j)},D^{(j)},P^{(j)},Q^{(j)},A^{(\mathrm{P}_j)},B^{(\mathrm{P}_j)},C^{(\mathrm{P}_j)},D^{(\mathrm{P}_j)},P^{(\mathrm{P}_j)},Q^{(\mathrm{P}_j)}\right]^{T}\\&=N_3\left[A^{(j-1)},B^{(j-1)},C^{(j-1)},D^{(j-1)},P^{(j-1)},Q^{(j-1)}\right]^{T}\end{aligned}, \quad (8)$$

where N_2 and N_3 are the 12×12 and 12×6 matrices, respectively. They are given in Appendix A. From Eq.(8), we obtain

$$\begin{aligned}&\left[A^{(j)},B^{(j)},C^{(j)},D^{(j)},P^{(j)},Q^{(j)},A^{(\mathrm{P}_j)},B^{(\mathrm{P}_j)},C^{(\mathrm{P}_j)},D^{(\mathrm{P}_j)},P^{(\mathrm{P}_j)},Q^{(\mathrm{P}_j)}\right]^{T}\\&=N_4\left[A^{(j-1)},B^{(j-1)},C^{(j-1)},D^{(j-1)},P^{(j-1)},Q^{(j-1)}\right]^{T}\end{aligned}. \quad (9)$$

From Eq. (9), we get

$$\mathbf{k}_L^{(j)}=N_5\mathbf{k}_R^{(j-1)},\quad j=2,3\cdots 26, \quad (10)$$

where $\mathbf{k}_L^{(j)}$ and $\mathbf{k}_R^{(j-1)}$ indicate the coefficient vectors in the left interface of the j^{th} region and the right interface of the (j-1)$^{\text{th}}$ region, respectively. N_5 is obtained by selecting the first to sixth rows of the matrix N_4 and has included the contribution of the

pillared resonator.

For the j^{th} region with a length s, the relationship between the state vector and coefficients vector can be expressed as

$$\mathbf{v}_R^{(j)} = N_6 \cdot \mathbf{k}_L^{(j)}, \quad j = 2,3\cdots 25, \tag{11}$$

where N_6 is the transfer matrix for waves propagating from the left to the right interface of the j^{th} region and it is shown in Appendix A. From Eqs. (7), (10) and (11), for waves propagating from the right interface of the $(j\text{-}1)^{\text{th}}$ region to the right interface of the j^{th} region, the transfer matrix can be expressed as

$$\mathbf{k}_R^{(j)} = N_1^{-1}\mathbf{v}_R^{(j)} = N_1^{-1}N_6\mathbf{k}_L^{(j)} = N_1^{-1}N_6N_5\mathbf{k}_R^{(j-1)}, \quad j = 2,3\cdots 25. \tag{12}$$

From Eq. (12), for waves propagating from the right interface of the 1st region to the right interface of the 25th region, the transfer matrix can be expressed as

$$\mathbf{k}_R^{(25)} = N_1^{-1}N_6N_5\mathbf{k}_R^{(24)} = (N_1^{-1}N_6N_5)^{24}\mathbf{k}_R^{(1)}. \tag{13}$$

Furthermore, for waves propagating from the right interface of the 1st region to the left interface of the 26th region, we get

$$\mathbf{k}_L^{(26)} = N_5\mathbf{k}_R^{(25)} = N_5(N_1^{-1}N_6N_5)^{24}\mathbf{k}_R^{(1)}. \tag{14}$$

From this equation, we can solve the amplitude and phase shift for the flexural wave propagating through these 25 pillared resonators. Eq. (14) can be rewrittend as

$$\mathbf{k}_{\text{out}} = N_5(N_1^{-1}N_6N_5)^{24}\mathbf{k}_{\text{in}}. \tag{15}$$

where $\mathbf{k}_{\text{in}} = \left[1, r_b, 0, r_b^*, 0, r_l\right]^T$, $\mathbf{k}_{\text{out}} = \left[t_b, 0, t_b^*, 0, t_l, 0\right]^T$, r_b, r_b^* and r_l are the amplitude ratios of the reflected propagating flexural wave in the 1st regions, respectively, t_b, t_b^* and t_l are the transmitted propagating flexural wave, transmitted evanescent flexural wave and transmitted longitudinal wave in the 26th

regions, respectively. From Eq. (15), r_b, t_b, r_b^*, t_b^*, r_l, and t_l can be solved. The phase shift of the transmitted wave is obtained by subtracting the phase in the right of the subunit from the phase in the left. More coresponding details can be found in Appendix A.

Fig. 3(d) shows the analytical amplitude (red line) and phase shift (blue line) of transmitted waves predicted by Eqs. (15) and **Erreur ! Source du renvoi introuvable.**. It can be seen that the phase shift with the high transmission (average over 0.8) by varying the pillar height can span over a full phase range of 2π. To evaluate the accuracy of the analytical solution, the simulated results obtained by COMSOL MULTIPHYSICS 5.4 software (Plane Strain Module) are shown with small circles and triangles in Fig. 3(d). The simulated results are in very good agreement with the analytical ones. This confirms the accuracy of the analytical method. It should be pointed out that the total thickness of the subunit L=49 mm is about half of the incident wavelength λ =98.9 mm [47], that is, these 25 pillared resonators constitute the sub-wavelength subunit.

2.3. The design of 3D subunits with the CII

The above-designed subunit is embodied in its 2D model, as shown in Fig. 3(a). The corresponding 3D one is shown in Fig. 4(a). The periodic boundary conditions need to be applied on the two long boundaries in the 3D strip-like subunit model. In order to display intuitively the 3D subunit applied by the periodic boundaries, another form is shown in Fig. 4(b). In our previous paper [33], slots are made at the subunit region (marked with the red dotted box in Fig. 4(a)) to avoid the CI. In the present work, we

retain the spacing in the 3D subunits instead of the slot. In this way, the CI between identical subunits (CII) will exist by the spacing, marked with red arrows in Fig. 4(b).

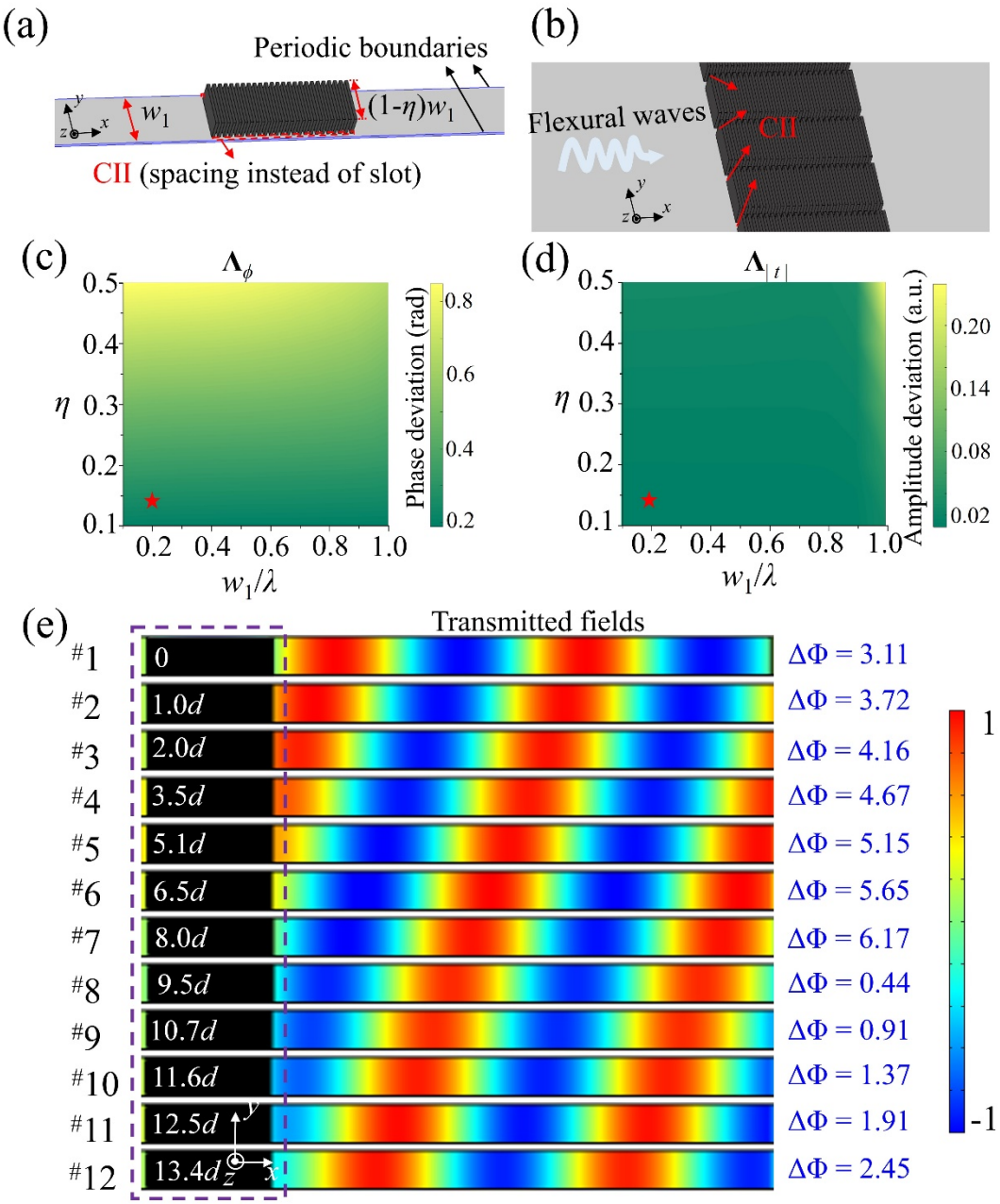

Fig. 4. (a) the 3D subunit. (b) Another form of the subunit applied by the periodic boundaries (c) and (d) the dependence of the influence coefficients Λ_ϕ and $\Lambda_{|t|}$ on w_1 and η. (e) illustrates the out-of-plane (z component) displacement distributions in transmitted fields for the twelve specific 3D subunits with the pillar height values marked in the left black square. The phase

shits for every subunit, which are obtained by subtracting the phase in the right of the subunit from the phase in the left, are marked in the right.

The spacing size is determined by the parameters of the subunit width w_1 and the filling ratio η, which is the ratio of the spacing width to the subunit width in one subunit. We need to analyze the influence of the CII, which is related to the subunit width w_1 and the filling ratio η, on the consistency of the single 3D subunit and the corresponding 2D subunit. The consistency of the single 3D subunit and the corresponding 2D subunit can be reflected in the differences between their phase shift and transmission amplitude for the different height h. Therefore, in the fixed design frequency, the phase shift ϕ_1 and transmission amplitude $|t_1|$ for the 3D subunits can be expressed as $\phi_1=G_{\phi 1}(w_1, \eta, h)$ and $|t_1|= G_{|t1|}(w_1, \eta, h)$, respectively, while that for the 2D subunits can be expressed as $\phi_0=G_{\phi 0}(h)$ and $|t_0|= G_{|t0|}(h)$, respectively. In order to quantitatively evaluate the influence of the CII, related to the subunit width w_1 and the ratio η, on the consistency of the 3D and 2D subunits, we define the influence coefficient as:

$$\Lambda_{\phi}\left(w_1,\eta\right)=\frac{1}{n}\cdot\sum_{h=d}^{n\cdot d}\left[G_{\phi_1}\left(w_1,\eta,h\right)-G_{\phi_0}\left(h\right)\right]$$

$$\Lambda_{|t|}\left(w_1,\eta\right)=\frac{1}{n}\cdot\sum_{h=d}^{n\cdot d}\left[G_{|t_1|}\left(w_1,\eta,h\right)-G_{|t_0|}\left(h\right)\right] \quad , \qquad (16)$$

where n=13, which is the ratio of the maximum pillar height (considered in Fig. 3d) to the thickness of the plate. The dependence of the influence coefficients Λ_{ϕ} and $\Lambda_{|t|}$ on w_1 and η are shown numerically in Figs. 4(c) and 4(d). It can be clearly seen that these two influence coefficients (determine the influence of CII) are small when the values of w_1 and η (determine the spacing size) are small. According to Figs. 4(c) and

4(d), w_1 and η are set as 0.2λ and 1/7, respectively (marked with the red stars). It can keep the consistency of the 3D and 2D subunits.

After the values of w_1 and η are set, in order to intuitively demonstrate the consistency, twelve specific 2D subunits are selected to achieve twelve steps of an equally phase shift to cover a full range of 2π according to Fig. 3(d). The corresponding out-of-plane (z component) displacement distributions in the transmitted field for the 3D subunits are plotted, as shown in Fig. 4(e). The black squares represent different subunits, and they are marked with the corresponding values of pillar heights. It can be observed from Fig. 4 (e) that twelve steps of an equal phase shift can still approximately cover a full range of 2π, and the transmitted fields are the uniformly high transmission. The values of phase shifts for every subunit, which are obtained by subtracting the phase in the right of the subunit from the phase in the left, are marked in the right of Fig. 4(e). Compared with Fig. 3(d), the average error of the phase shifts is very small (about 0.1 rad). It, indeed, indicates that the CII has little effect on the consistency of the designed 3D and corresponding 2D subunits.

3. The constructive and destructive interferences between the adjacent different subunits

The above twelve 3D subunits in the order shown in Fig. 4(e) are integrated into a supercell as shown in Fig. 5(c). Two identical supercells, providing a stair-step (linearly gradient) discrete phase profile, compose the elastic metasurfaces in Figs. 5(a) and 5(b). For these two metasurfaces, the only difference between them is that one has no CI (with a slot) at the junction of the supercells and the other has CI (without a slot), as

shown in the upper right corners of Figs. 5(a) and 5(b). The simulations of deflected flexural wave fields by the two metasurfaces are shown in Figs. 5(a) and 5(b). It can be clearly seen in Fig. 5(a) that the incident wave is deflected without any undesired distortion in the transmitted field. However, in Fig. 5(b), the transmitted field near the junction of two supercells is destroyed. The upper part of the transmitted field is hardly deflected. By comparing these two simulation results, we know that the destruction of the transmitted field is mainly due to the CI at the junction of the two supercells.

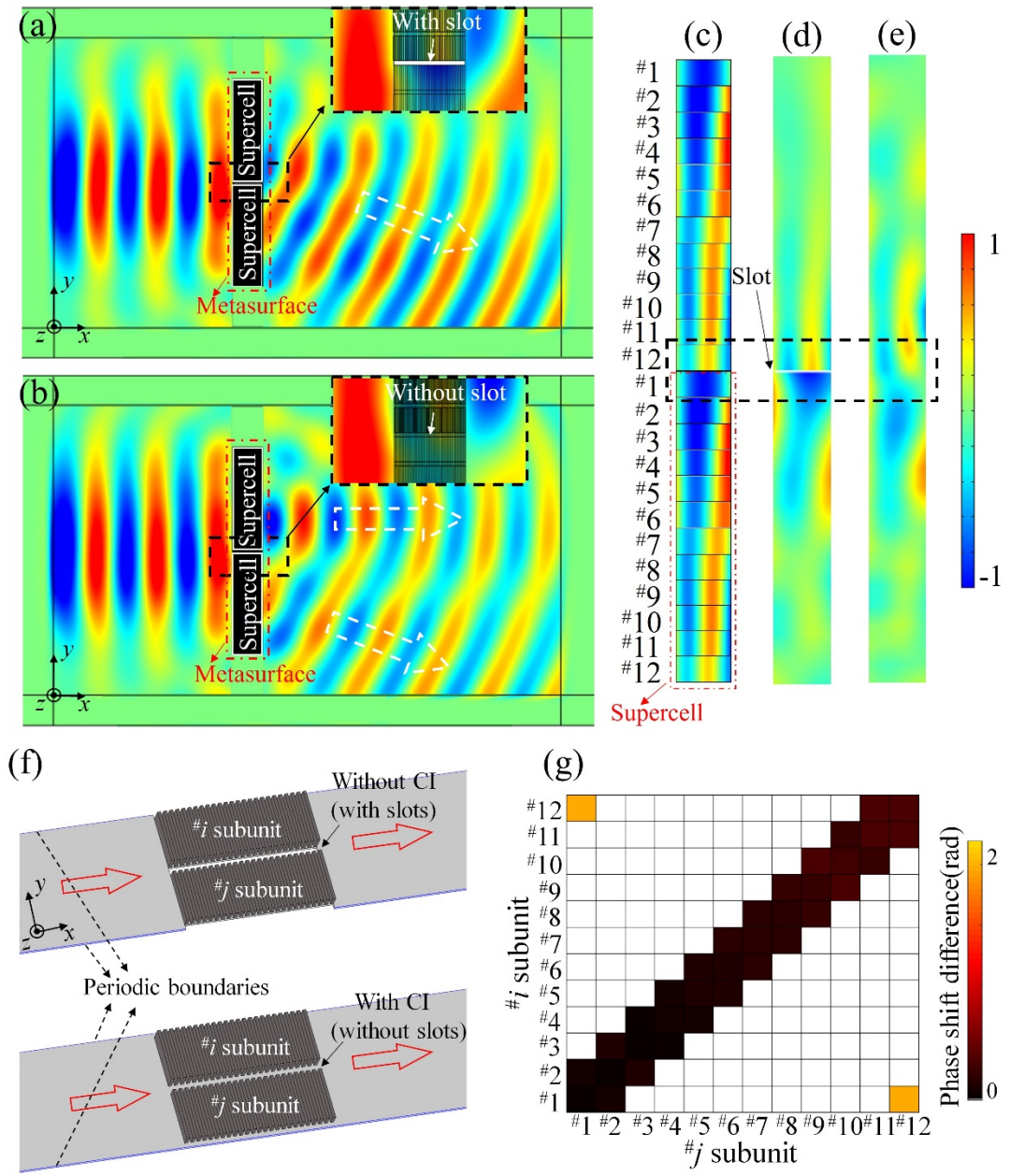

Fig. 5. (a) and (b) illustrate the two metasurfaces consist of two supercells. Enlarged views of the junctions of adjacent supercells, with slot and without slot, are shown in the back dotted frames in upper right corners of (a) and (b). (c) illustrates OWMS for the twelve black squares (the 3D subunits) shown in Fig. 4(e). (d) and (e) illustrate OWMS for the black squares (the supercells) shown in (a) and (b). (f) The models are composed of two subunits with different heights. The one has slots and the other has no slots. (g) shows the deviation between the phase shifts for the two models in (f).

The subunit consists of the square pillars and the plate under them, shown in Fig.

4(a), which are named as subunit pillars and subunit plate, respectively, for easy description. In order to reveal the intrinsic physics, the out-of-plane wave fields (*z* components of the displacements) on the mid-planes of subunit plates (OWMS), corresponding to the twelve black squares (the 3D subunits) in Fig. 4(e), are extracted, as shown in Fig. 5(c). It can be observed for one supercell that the difference of the extracted OWMSs between adjacent subunits from the $^{\#}1$ subunit to the $^{\#}12$ subunit is small. After the two supercells are arranged to design the metasurface, Fig. 5(c) shows the $^{\#}1$ subunit in the lower supercell and the $^{\#}12$ subunit in the upper supercell become adjacent two subunits, marked with black dotted box in Fig. 5(c). It can be seen that the difference of OWMSs between the two subunits is large, especially in terms of wave intensity and wavelength size. For example, the wave intensity for the $^{\#}1$ subunit is about 2.5 times of that for the $^{\#}12$ subunit, which may be caused by the different energy diversions of pillared resonators with different heights. Furthermore, Fig. 5(c) shows approximate one and a half wavelength for the $^{\#}12$ subunit and a half wavelength for the $^{\#}1$ subunit. This means one third of the particles in the adjacent subunit plates move in opposite directions. The very different OWMSs for the two subunits will be superimposed to form a new mixed wave field through the vibrations of plate at the junction, i.e., CI. In other words, the CI from the junction of the two adjacent subunits, which have very different OWMSs, greatly destroys their designed wave fields.

Furthermore, the OWMSs corresponding to the black squares (the supercells) in Figs. 5(a) and 5(b), are extracted, respectively, as shown in Figs. 5(d) and 5(e). Since the incident wave is a Gauss beam, the wave intensity decreases gradually from the

middle to the outsides. In Fig. 5(d), the CI exists between all two adjacent subunits within the supercell, but not between the two outer ones in different supercells (the $^{\#}1$ subunit in the lower supercell and the $^{\#}12$ subunit in the upper supercell). Compared with OWMSs in Fig. 5(c), that in Fig. 5(d) are almost the same. It confirms that the CI within a supercell causes constructive interference due to smaller different OWMSs between the adjacent subunits. This will result in fine wave field manipulation. In Fig. 5(e), the CI exists in all adjacent subunits including the junction between the $^{\#}1$ subunit in the lower supercell and the $^{\#}12$ subunit in the upper supercell. Compared with OWMSs in Fig. 5(c), that in Fig. 5(e) has changed a lot, specially at the junction (back dotted frame). It confirms that the CI at the junction of two supercells causes destructive interference due to larger different OWMSs between the adjacent subunits. This will result in bad wave field manipulation.

To further quantitatively analyze the influence of the CI on the designed subunits, we select all adjacent two subunits, i.e., $^{\#}i$ subunit and $^{\#}j$ subunit, from the two supercell in Fig. 5(c). The values of i and $j = i \pm 1$ are set to make the two subunits as the adjacent ones. The two adjacent subunits make up the two types of analytical models, the one has the slots and the other has no slots, as shown in the upper and lower subplots of Fig. 5(f), respectively. For the two types of analytical models, we calculate the transmitted fields and obtain the phase shift in the far field, respectively. For the first type of model with slots, the obtained phase shifts are accurate values without the influence of the CI on the OWMSs. For the second type of model without slots, there will be some deviation in the obtained phase shifts due to the influence of CI on the

OWMSs. The difference values between the phase shifts for the two types of models are shown in Fig. 5(g). It can quantitatively analyze the influence of CI on OWMSs, which will determine the manipulation effect of the transmitted field. In order to make a comprehensive comparison, we also add the phase shift differences for the models composed of two identical subunits ($i = j$) to Fig. 5(g), which are related to the 3D subunits applied by the periodic boundaries.

It can be clearly observed that the phase shift difference for the model composed of the #1 subunit and the #12 subunit reaches a large value of 2 rad, while the remaining differences are all less than 0.4 rad. The big difference value of 2 rad indicates that the transmitted wave field has been completely destroyed by the CI, the small difference value less than 0.4 rad indicates that the CI results in constructive interference. We can know from the above analysis of Fig. 5(c) that only the OWMSs between the subunit 1 and the subunit 12 in all adjacent subunits have big difference while the OWMSs for all other adjacent subunits have a small difference. It indicates that the CI between two adjacent subunits with very different OWMSs will lead to destructive interference while the CI between two subunits with small different OWMSs will lead to constructive interference. Therefore, we can take the advantage of the constructive interference to avoid having slots in the subunits.

4. Manipulating flexural waves by the PEMC

To design the PEMC, we need to take the advantage of the constructive interference and avoid the destructive one. For the deflecting metasurface, continuous phase shift within one supercell and an abrupt phase shift of 2π between two adjacent

supercells will make wave front linear change in the transmitted filed due to the wave periodicity [12]. The OWMSs for the two adjacent subunits at the junction between the two adjacent supercells exhibit a larger difference and that for other two adjacent ones have a small difference. It will lead to the constructive interference exist all two adjacent subunits, except for that at the junction between the adjacent supercells. Therefore, in the present study, taking the advantage of the constructive interference and avoiding the destructive one, we can just use one supercell without any slots to build the deflecting PEMC. It should be pointed out that this has one limitation, i.e., it is only suitable for incident Gauss beam whose width does not exceed the width of one supercell. However, we can simply eliminate this limitation by introducing only one slot at the junction of adjacent two supercells, which still greatly reduces the damage to the plate. However, for the focusing PEMC, there is no such limitation. The reason is that the phase shift for all two adjacent subunits is continuous without the abrupt phase shift. It enables our new conceptual design to be of great value for the focusing metasurface.

4.1. Sample fabrication and experimental setup

To accurately fabricate the iron pillared resonator, the Wire Electrical Discharge Machining (WEDM) with a manufacturing precision of 0.01 mm is adopted. The manufactured iron pillared resonators are bonded to the middle of the aluminum alloy plate (1000 mm × 2000 mm × 1 mm) by a special adhesive. The enlarged view of the deflecting PEMC sample is shown in the top of Fig. 1(a). An array of four piezoelectric patches PZT-5A (20 mm × 20 mm × 0.3 mm) is bonded on the surface of the plate

acting as actuators. The spacing of adjacent piezoelectric patches is set as the width of the piezoelectric patch according to the phased array theory [2]. By rotating the direction of the bonded piezoelectric patch array, we can get different incident angles. The exciting frequency is 1 kHz and the value of f·d (the product of the frequency and the plate thickness) is far less than 0.4 MHz mm [48]. Normal traction excitation of the piezoelectric patches can be used to generate a flexural wave (single Lamb mode A0) with the high signal-to-noise ratio.

With the controlling of the waveform editor (based on the Labview software), the signal generator (Agilent 33220A) generates a 5-cycle tone burst signal $w_t = A_0\left[1-\cos\left(2\pi f_c t/5\right)\right]\sin\left(2\pi f_c t\right)$, where $f_c = 1$ kHz is the central frequency. The power amplifier (HVPA05) drives the piezoelectric patches in a manner that the amplified voltage for the two middle piezoelectric patches is two times of that for the ones on both sides. The bonded four piezoelectric patches can approximately excite the transient flexural wave Gaussian beam. A layer of blue-tack is glued on the boundary edges to minimize reflections from the outer boundary of the test piece [22, 23]. The wave fields in the incident and transmitted areas are measured by the PSV-400 scanning laser Doppler vibrometer. In the scanning areas, more than six points in one flexural wavelength need to be scanned to ensure fine resolution.

4.2 PEMC for deflecting flexural waves

The PEMC without slots is formed by one supercell, as shown in Fig. 1(a). According to the GSL, the theoretical refraction angle θ_t of the incident wave can be calculated by

$$\theta_t = \arcsin\left[\sin\theta_i + \frac{\lambda}{2\pi}\cdot\frac{d\phi}{dy}\right], \tag{17}$$

where θ_i is the incident angle. $d\phi/dy = 2\pi/(12w_1) = 26.18$ is the spatial phase shift gradient. Firstly, a vertically incident flexural wave is considered, i.e., $\theta_i = 0$. In the supercell, the phase shift of subunits is set to increase along the opposite direction of the *y*-axis. The theoretical refraction angle of the transmitted wave is calculated to be 24.3° according to Eq. (17). For obliquely incident flexural wave, when the incident angle meets with the relationship of $\sin\theta_i < (\lambda/2\pi)\cdot(d\phi/dy)$, and the phase shift of subunits is set to increase along the *y*-axis, negative refraction will occur. As a typical example, the incident angle is set as $\theta_i = 15^\circ$, the corresponding theoretical refraction angle is calculated to be -8.8°.

The corresponding numerical simulations are carried out. The simulation results are shown in Figs. 6(a) and 6(c). It can be clearly observed that the vertically and obliquely incident waves have been deflected by the designed PEMC and the negative refraction appears in the transmitted field in Fig. 6(c). In order to get the refraction angle from the numerical simulations, polar directivity graphs of the transmitted waves measured at two wavelengths away from the center of the PEMCs are shown in Figs. 6(b) and 6(d). It can be observed that the refraction angles are 25.1° and -9.6°, respectively, which have a good agreement with the theoretical ones, recalling that the corresponding angles are 24.3°and -8.8°.

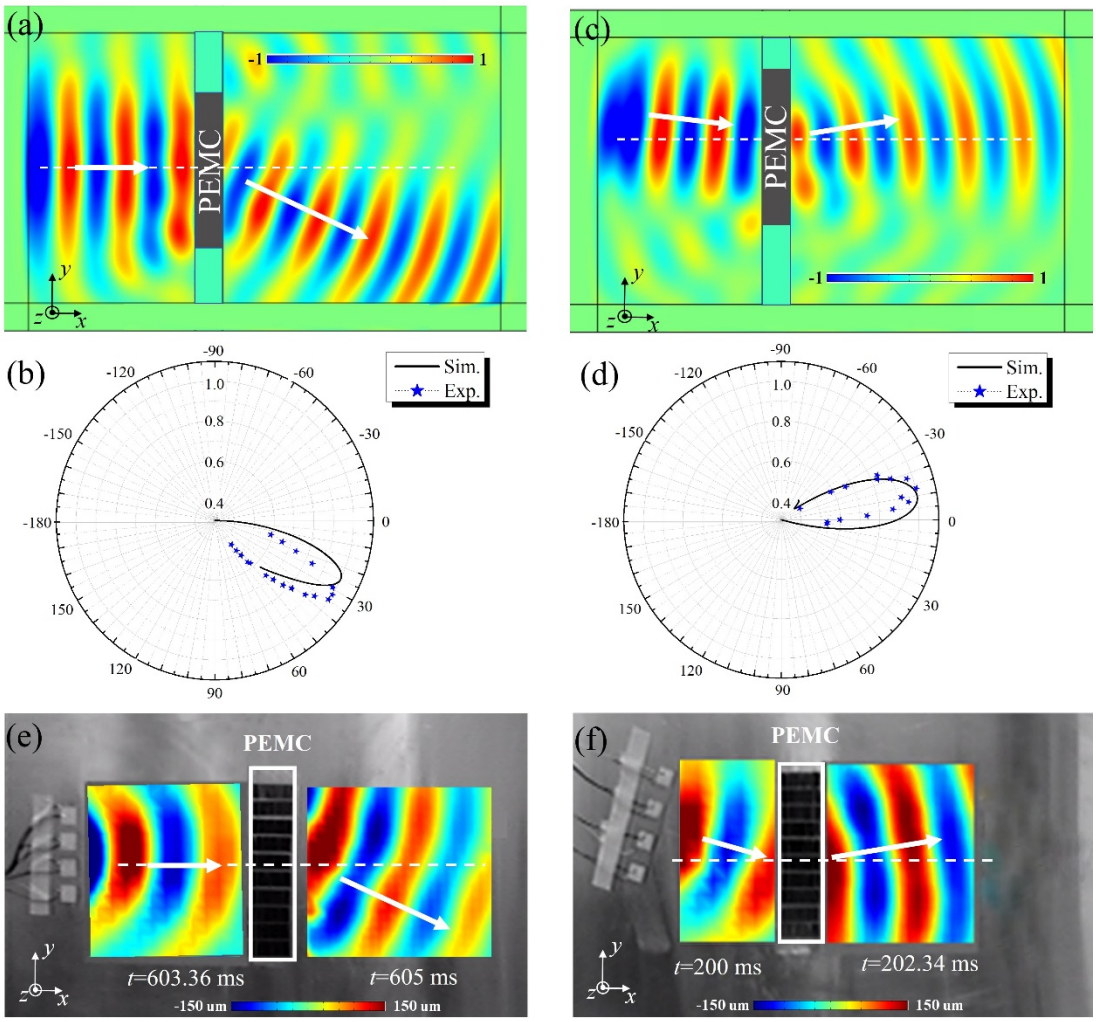

Fig. 6. The numerical simulation results for the vertically (a) and obliquely (c) incident waves across the PEMC. Polar directivity graphs of the transmitted waves measured at two wavelengths away from the center of the PEMCs are shown in (b) and (d), numerically and experimentally. The experimental full wave fields including the incident field and the transmitted field at different time points are shown in (e) and (f).

In order to show the deflection intuitively, the experimental full wave fields in the incident and transmitted zones at different time points are shown in Figs. 6(e) and 6(f) by the "time" measurement mode. The time points of measurements for the incident and transmitted wave fields are marked below the wave fields. For example, in Fig. 6(e), the incident field and the transmitted field are measured at 603.36 ms and 605 ms,

respectively. From the two test results, it can be clearly observed that the designed PEMC can abnormally deflect the vertically and obliquely incident flexural waves. In order to obtain the experimental refraction angles, firstly, the maximum peak values of 5-cycle tone burst signal for every measured point at two wavelengths away from the center of the PEMCs are searched in the whole test process. Then, based on maximum peak values, the polar directivity graphs of the transmitted waves across the specimen are added to Figs. 6(b) and 6(d). The experimentally observed angles from the polar directivity graphs are 31.2°and -12.1°, respectively, recalling that the corresponding simulation angles are 25.1°and -9.6°. These experimental results for deflecting PEMC are in good agreement with both the theoretical and numerical simulation results. Some small deviations mainly come from the manufacturing error of the specimen and the measurement noise.

4.3. PEMC for focusing flexural waves

The focusing PEMC without slots is illustrated in the upper right corner of Fig. 7(a). It can be readily constructed by selecting subunits that match the requested hyperbolic phase profile $\phi(y)=\frac{2\pi}{\lambda}(\sqrt{\hat{F}^2+y^2}-\hat{F})$, where $\hat{F}$ is the designed focal distance. Without loss of generality, the focal distance is set as $\hat{F}=3\lambda$. The continuous phase profile makes the pillar height in the PEMC changes gradually. According to Fig. 3(d), the corresponding values of the pillar heights for all subunits with the precision of 0.1mm are presented by Table B1 in Appendix B. The metasurface with gradually changing of the subunits will lead to the OWMSs change gradually. There

is not a very different OWMS between adjacent subunits. Therefore, for all adjacent subunits, there are constructive interferences.

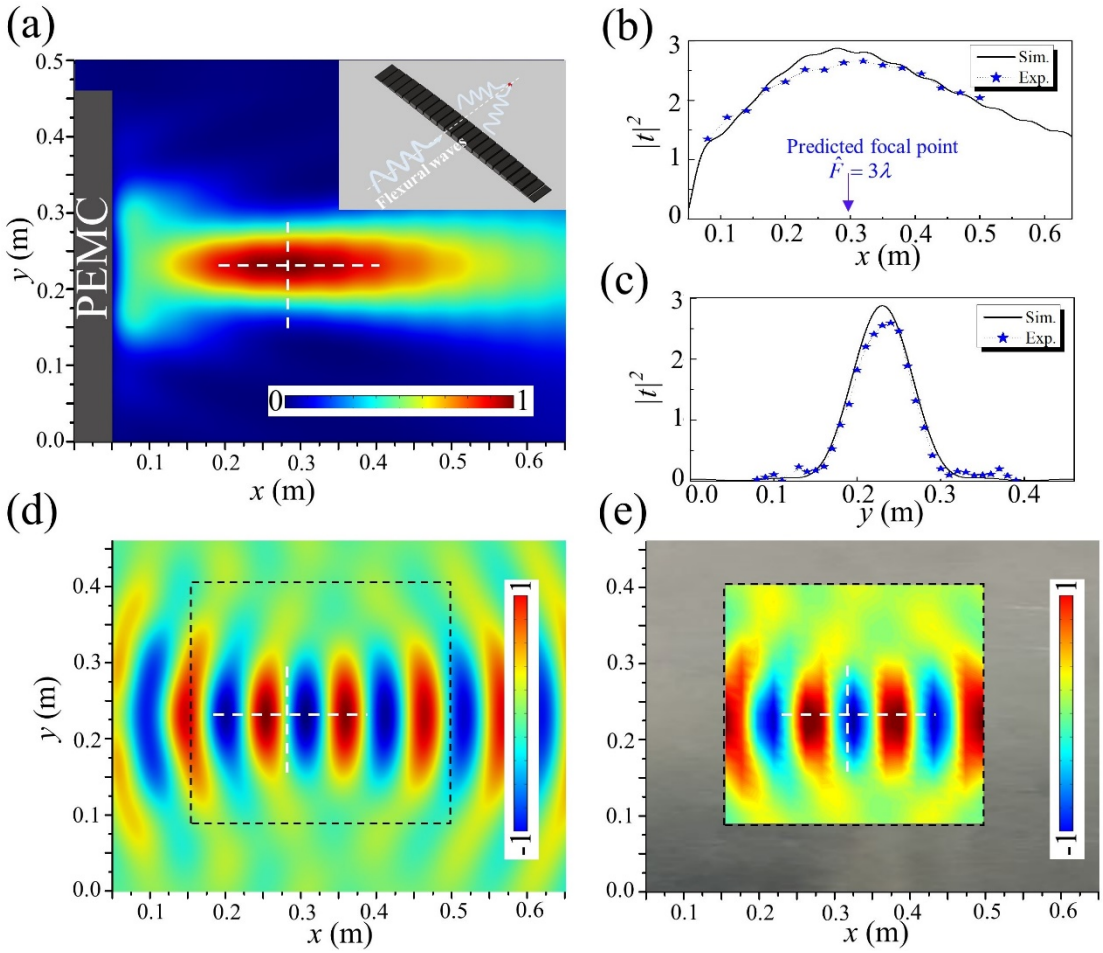

Fig. 7. (a) shows the transmitted field of incident flexural waves propagating through the PEMC capable of focusing. The intersection (of white dashed lines) points out the predicted position of the focal point. The model of the PEMC is illustrated in the upper right corner. (b) and (c) show the intensity distribution of normalized amplitude along the longitudinal dashed line and transverse dashed line in (a) from the simulation and experiment, respectively. (d) and (e) show the displacement fields of the simulation and experiment, respectively.

The transmitted intensity and displacement fields with the focal distance of 3λ is simulated and shown in Figs. 7(a) and 7(d), respectively. One can clearly observe a focal spot after the incident waves go passing through the PEMC. The theoretically

predicted position of the designed focusing point is located at the intersection of the longitudinal and transverse dashed lines, as shown in Fig. 7(a). The full field of experimental measurement is shown in Fig. 7(e), which is normalized by the incident wave field. The transmitted energy is proportional to the square of the displacement amplitude [49]. The normalized energy intensity can be expressed as $|t|^2$, which is the ratio of the square of the displacement amplitude in the transmitted filed to that in the incident field. For a more quantitative comparison, the normalized energy intensity distribution along the longitudinal dashed line from the simulations and experiments is also plotted in Fig. 7(b). It can be seen that the energy intensity of the peak is about 3. The normalized energy intensity distribution at the focal spot along the transverse dashed line from the simulations and experiments is also plotted in Fig. 7(c). As one can observe, the peaks from the simulations and experiments approximately occur at the targeted focal distance of $x \approx 3\lambda$. The experimental result for focusing PEMC is in good agreement with both the theoretical and numerical simulation results, although some small deviations exist due to the manufacturing error of the specimen and the measurement noise.

5. Conclusions

For the improved subunits (~0.495λ), the lowest dispersion band and vibration mode analysis reveal the mechanism of phase shift, that is, arrayed pillared resonators decrease the wavenumber of the flexural wave in the subunit due to slowing down. The corresponding analytical model is established and both of the amplitude and the phase shift of transmitted waves across the subunits are analytically solved. In addition, we

have revealed that the CI between the two subunits with larger different OWMSs lead to destructive interference, while the CI between the two subunits with smaller different OWMSs lead to the constructive interference. Further, combined with the constructive interference, pillared elastic metasurfaces have been analytically and numerically investigated to manipulate incident flexural waves in a plate. We find that the subwavelength focusing PEMC (~0.495λ) enables our new conceptual design to be of great value because has only the constructive interference due to the continuous phase shift for every two adjacent subunits. Finally, we experimentally have demonstrated the deflecting and focusing functionalities of the designed PEMC. This proposed conceptual design can ensure the integrity of the original plate without introducing any damage to its strength and stiffness. We expect the present work will open a new avenue for a variety of applications in the field of elastic metamaterials/ metasurfaces with the constructive interference.

Acknowledgment

This project is supported by the National Natural Science Foundation of China (Grant No.11972296), the 111 Project (No. BP0719007), the Institute CARNOT (ICEEL), La Région Grand Est, the Fundamental Research Funds for the Central Universities (No. 310201901A005). The first author is grateful to the support of Innovation Foundation for Doctor Dissertation of Northwestern Polytechnical University (Grant No. CX201936) and China Scholarship Council (CSC No. 201806290176).

Appendix A: Boundary conditions and the transfer matrixes

In Fig. 3(c), the positive directions of axial force F, shear force V and bending moment M are marked at the interfaces among the $(j\text{-}1)^{th}$ region, j^{th} region, and j^{th} pillared resonator [50, 51]. The force and moment must be balanced at the connection position. According to Fig.3(c), the following boundary conditions must be satisfied.

Force balance in x direction:

$$F^{(j-1)} - F^{(j)} + V^{(\mathrm{P}_j)} = 0 \tag{A1}$$

Force balance in z direction:

$$V^{(j-1)} - V^{(j)} - F^{(\mathrm{P}_j)} = 0 \tag{A2}$$

Moment balance:

$$M^{(j-1)} - M^{(j)} - M^{(\mathrm{P}_j)} = 0 \tag{A3}$$

At the connection position, the displacement and rotation angle are continuous, so the following boundary conditions must be satisfied.

Displacement continuity in x direction:

$$u^{(j-1)} = u^{(j)} \tag{A4}$$

$$u^{(j-1)} = -w^{(\mathrm{P}_j)} \tag{A5}$$

Displacement continuity in z direction:

$$w^{(j-1)} = w^{(j)} \tag{A6}$$

$$w^{(j-1)} = u^{(\mathrm{P}_j)} \tag{A7}$$

Slope continuity:

$$\varphi^{(j-1)} = \varphi^{(j)} \tag{A8}$$

$$\varphi^{(j-1)} = \varphi^{(\mathrm{P}_j)} \tag{A9}$$

At the top of the j^{th} pillar resonator ($z = h$), there is no constraint, hence the force and moment are 0.

$$V^{(P_j)}\Big|_{z=h} = 0 \tag{A10}$$

$$F^{(P_j)}\Big|_{z=h} = 0 \tag{A11}$$

$$M^{(P_j)}\Big|_{z=h} = 0 \tag{A12}$$

The relationships between the slope φ and the displacement w, between axial force F and the displacement u, between shear force V and the displacement w, between bending moment M and the displacement w are:

$$\begin{aligned} &\varphi = w' \\ &F = \frac{Ed}{(1-\nu^2)}u', \\ &V = -EIw''' \\ &M = EIw'' \end{aligned} \tag{A13}$$

respectively, where the superscript $'$ indicates space differentiation with respect to the corresponding coordinate.

The transformation matrix between the state vector and the coefficient vector N_1 is:

$$N_1 = \begin{bmatrix} 1 & 1 & 1 & 1 & 0 & 0 \\ 0 & 0 & 0 & 0 & 1 & 1 \\ -ik_{b1} & ik_{b1} & -k_{b1} & k_{b1} & 0 & 0 \\ 0 & 0 & 0 & 0 & -ik_{l1}E_1H_1 & ik_{l1}E_1H_1 \\ -iE_1I_1k_{b1}^3 & iE_1I_1k_{b1}^3 & -E_1I_1k_{b1}^3 & E_1I_1k_{b1}^3 & 0 & 0 \\ -E_1I_1k_{b1}^2 & -E_1I_1k_{b1}^2 & E_1I_1k_{b1}^2 & -E_1I_1k_{b1}^2 & 0 & 0 \end{bmatrix}, \tag{A14}$$

where $H_1 = d_1 / (1 - \nu_1^2)$.

The transfer matrix N_2 has the following components:

$T_{15} = -12ik_{l1}E_1I_1 / h_1^2$, $T_{16} = 12ik_{l1}E_1I_1 / h_1$, $T_{17} = iE_2I_2k_{b2}^3$, $T_{18} = -iE_2I_2k_{b2}^3$, $T_{19} = -E_2I_2k_{b2}^3$, $T_{110} = E_2I_2k_{b2}^3$, $T_{21} = -iE_1I_1k_{b1}^3$, $T_{22} = iE_1I_1k_{b1}^3$, $T_{23} = E_1I_1k_{b1}^3$,

$T_{24}=-E_1I_1k_{b1}^{\ 3}$, $T_{211}=\text{-}ik_{l2}E_2I_2/h_2^{\ 2}$, $T_{212}=ik_{l2}E_2I_2/h_2^{\ 2}$, $T_{31}=-E_1I_1k_{b1}^{\ 2}$,

$T_{32}=-E_1I_1k_{b1}^{\ 2}$, $T_{33}=E_1I_1k_{b1}^{\ 2}$, $T_{34}=E_1I_1k_{b1}^{\ 2}$, $T_{37}=-E_2I_2k_{b2}^{\ 2}$, $T_{38}=-E_2I_2k_{b2}^{\ 2}$,

$T_{39}=E_2I_2k_{b2}^{\ 2}$, $T_{310}=E_2I_2k_{b2}^{\ 2}$, $T_{45}=-1$, $T_{46}=-1$, $T_{57}=1$, $T_{58}=1$, $T_{59}=1$,

$T_{510}=1$, $T_{61}=1$, $T_{62}=1$, $T_{63}=1$, $T_{64}=1$, $T_{711}=1$, $T_{712}=1$, $T_{81}=\text{-}ik_{b1}$, $T_{82}=ik_{b1}$,

$T_{83}=-k_{b1}$, $T_{84}=k_{b1}$, $T_{97}=-ik_{b2}$, $T_{98}=ik_{b2}$, $T_{99}=-k_{b2}$, $T_{910}=k_{b2}$,

$T_{107}=\text{-}iE_2I_2k_{b2}^{\ 3}e^{\text{-}ik_{b2}h}$, $T_{108}=iE_2I_2k_{b2}^{\ 3}e^{ik_{b2}h}$, $T_{109}=E_2I_2k_{b2}^{\ 3}e^{\text{-}k_{b2}h}$, $T_{128}=-E_2I_2k_{b2}^{\ 2}e^{ik_{b2}h}$,

$T_{129}=E_2I_2k_{b2}^{\ 2}e^{\text{-}k_{b2}h}$, $T_{1010}=-E_2I_2k_{b2}^{\ 3}e^{k_{b2}h}$, $T_{1210}=E_2I_2k_{b2}^{\ 2}e^{k_{b2}h}$, $T_{1112}=ik_{l2}E_2I_2/h^2e^{ik_{l2}h}$,

$T_{129}=E_2I_2k_{b2}^{\ 2}e^{\text{-}k_{b2}h}$, $T_{1111}=\text{-}ik_{l2}E_2I_2/h^2e^{\text{-}ik_{l2}h}$, others items equal zero.

The transfer matrix N_3 can be expressed as:

$$N_3=\begin{bmatrix} 0 & 0 & 0 & 0 & -ik_{l1}EH_1 & ik_{l1}EH_1 \\ -iEIk_{b1}^{\ 3} & iEIk_{b1}^{\ 3} & EIk_{b1}^{\ 3} & -EIk_{b1}^{\ 3} & 0 & 0 \\ -EIk_{b1}^{\ 2} & -EIk_{b1}^{\ 2} & EIk_{b1}^{\ 2} & EIk_{b1}^{\ 2} & 0 & 0 \\ 0 & 0 & 0 & 0 & -1 & -1 \\ 0 & 0 & 0 & 0 & -1 & -1 \\ 1 & 1 & 1 & 1 & 0 & 0 \\ 1 & 1 & 1 & 1 & 0 & 0 \\ -ik_{b1} & ik_{b1} & -k_{b1} & k_{b1} & 0 & 0 \\ -ik_{b1} & ik_{b1} & -k_{b1} & k_{b1} & 0 & 0 \\ 0 & 0 & 0 & 0 & 0 & 0 \\ 0 & 0 & 0 & 0 & 0 & 0 \\ 0 & 0 & 0 & 0 & 0 & 0 \end{bmatrix}. \tag{A15}$$

For the j^{th} region with a length s, waves propagate from the left to the right. From Eqs. (2), (3) and (A13), the relationship between the physical quantities $w_R^{(j)}$, $u_R^{(j)}$, $\varphi_R^{(j)}$, $F_R^{(j)}$, $V_R^{(j)}$, $M_R^{(j)}$ in the right interface of the j^{th} region and the complex coefficients $A_L^{(j)}$, $B_L^{(j)}$, $C_L^{(j)}$, $D_L^{(j)}$, $P_L^{(j)}$, $Q_L^{(j)}$ in the left interface of the j^{th} region can be expressed as follows:

$$w_R^{(j)} = A_L^{(j)}e^{-ik_{b1}s} + B_L^{(j)}e^{ik_{b1}s} + C_L^{(j)}e^{-k_{b1}s} + D_L^{(j)}e^{k_{b1}s}$$

$$u_R^{(j)} = P_L^{(j)}e^{-ik_{l1}s} + Q_L^{(j)}e^{ik_{l1}s}$$

$$\varphi_R^{(j)} = -ik_{b1}A_L^{(j)}e^{-ik_{b1}s} + ik_{b1}B_L^{(j)}e^{ik_{b1}s} - k_{b1}C_L^{(j)}e^{-k_{b1}s} + k_{b1}D_L^{(j)}e^{k_{b1}s}$$

$$F_R^{(j)} = -12ik_{l1}E_1I_1/d^2\ P_L^{(j)}e^{-ik_{l1}s} + 12ik_{l1}E_1I_1/d^2\ Q_L^{(j)}e^{ik_{l1}s} \quad . \quad \text{(A16)}$$

$$V_R^{(j)} = -iE_1I_1{k_{b1}}^3A_L^{(j)}e^{-ik_{b1}s} + iE_1I_1{k_{b1}}^3B_L^{(j)}e^{ik_{b1}s} + E_1I_1{k_{b1}}^3C_L^{(j)}e^{-k_{b1}s} - E_1I_1{k_{b1}}^3D_L^{(j)}e^{k_{b1}s}$$

$$M_R^{(j)} = -E_1I_1{k_{b1}}^2A_L^{(j)}e^{-ik_{b1}s} - E_1I_1{k_{b1}}^2B_L^{(j)}e^{ik_{b1}s} + E_1I_1{k_{b1}}^2C_L^{(j)}e^{-k_{b1}s} + E_1I_1{k_{b1}}^2D_L^{(j)}e^{k_{b1}s}$$

Here, $s = l_0 + \hat{d}_2$, Eq. (A16) can be rewritten in matrix form as follows:

$$\mathbf{v}_R^{(j)} = N_6 \cdot \mathbf{k}_L^{(j)}, \quad j = 2,3\cdots 25, \qquad \text{(A17)}$$

where N_6 is the transfer matrix for waves propagating from the left to the right interface of the j^{th} region and it is

$$N_6 = \begin{bmatrix} e^{-ik_{b1}s} & e^{ik_{b1}s} & e^{-k_{b1}s} & e^{k_{b1}s} & 0 & 0 \\ 0 & 0 & 0 & 0 & e^{-ik_{l1}s} & e^{ik_{l1}s} \\ -ik_{b1}e^{-ik_{b1}s} & ik_{b1}e^{ik_{b1}s} & -k_{b1}e^{-k_{b1}s} & k_{b1}e^{k_{b1}s} & 0 & 0 \\ 0 & 0 & 0 & 0 & -D_1e^{-ik_{l1}s} & D_1e^{ik_{l1}s} \\ -iD_2k_{b1}e^{-ik_{b1}s} & iD_2k_{b1}e^{ik_{b1}s} & D_2k_{b1}e^{-k_{b1}s} & -D_2k_{b1}e^{k_{b1}s} & 0 & 0 \\ -D_2e^{-ik_{b1}s} & -D_2e^{ik_{b1}s} & D_2e^{-k_{b1}s} & D_2e^{k_{b1}s} & 0 & 0 \end{bmatrix}, \qquad \text{(A18)}$$

where $D_1 = 12ik_{l1}E_1I_1/d^2$ and $D_2 = E_1I_1{k_{b1}}^2$. For accurately solving the phase shift, the modifying thickness of the pillared resonator $\hat{d}_2 = 0.9 \cdot d_2$ must be added to the length of the j^{th} region, which can compensate the ignored thickness of the pillared resonator in boundary conditions between the $(j\text{-}1)^{\text{th}}$ and j^{th} regions.

The wave fields for the 1st and 26th regions can be described as follows:

$$
\begin{aligned}
w^{(1)}(x) &= e^{-ik_{b1}x} + r_b e^{ik_{b1}x} + r_b^* e^{k_{b1}x} \\
u^{(1)}(x) &= r_l e^{ik_{l1}x} \\
w^{(26)}(x) &= t_b e^{-ik_{b1}x} + t_b^* e^{-k_{b1}x} \\
u^{(26)}(x) &= t_l e^{-ik_{l1}x}
\end{aligned}, \tag{A19}
$$

where $e^{-ik_{b1}x}$ is the incident flexural wave with an amplitude of 1, r_b, r_b^* and r_l are the amplitude ratios of the reflected propagating flexural wave, reflected evanescent flexural wave and reflected longitudinal wave in the 1st regions, respectively. t_b, t_b^* and t_l are the transmitted propagating flexural wave, transmitted evanescent flexural wave and transmitted longitudinal wave in the 26th regions, respectively. The coefficient vectors $\mathbf{k}_{\mathrm{R}}^{(1)}$ and $\mathbf{k}_{\mathrm{L}}^{(26)}$ are written as $\mathbf{k}_{\mathrm{in}}$ and $\mathbf{k}_{\mathrm{out}}$, respectively, in terms of $\mathbf{k}_{\mathrm{in}}=\left[1, r_b, 0, r_b^*, 0, r_l\right]^T$, $\mathbf{k}_{\mathrm{out}}=\left[t_b, 0, t_b^*, 0, t_l, 0\right]^T$.

The phase of t_b can be calculated by using the following formula:

$$
\phi_b = \begin{cases} \pi + \arctan\left(\dfrac{\mathrm{Imag}(t_b)}{\mathrm{Real}(t_b)}\right) & \text{if real}(t_b)<0 \\ \arctan\left(\dfrac{\mathrm{Imag}(t_b)}{\mathrm{Real}(t_b)}\right) & \text{if real}(t_b)>0 \end{cases}. \tag{A20}
$$

Appendix B: The sensitivity and limitation of the focusing PEMC

Table B1. The pillar height h_i (mm) (i=1, 2, …, 12) corresponding to focusing PEMCs with different precisions

h_i	h_{12}	h_{11}	h_{10}	h_9	h_8	h_7	h_6	h_5	h_4	h_3	h_2	h_1
Pr=0.1	13.3	13.2	13.0	12.7	12.2	11.6	10.8	9.6	8.0	6.3	4.4	2.3
Pr=0.5	13.5	13.0	13.0	12.5	12.0	11.5	11.0	9.5	8.0	6.5	4.5	2.5
Pr=1.0	13.0	13.0	13.0	13.0	12.0	12.0	11.0	10.0	8.0	6.0	4.0	2.0

For the focusing PEMC in Fig. 7(a), the values of the pillar heights in the subunits have a precision of 0.1 mm, as shown in the first row of Table B1. Further, the sensitivity of

the focusing PEMC is investigated by the designed errors of the pillar heights. To this end, we will carry out numerical studies on the focusing performance [the focal distance of 3λ with f = 1 kHz] to show the sensitivity to designed errors. The values of the pillar heights for two lower precisions (Pr = 0.5 and 1.0 mm) are presented in Table B1 by rounding each value of Pr = 0.1 mm up to the nearest value. By employing these pillar heights separately, the PEMCs are designed and the transmitted fields are simulated. The normalized transverse and longitudinal intensities at the focal spot along two orthogonal directions [white dashed lines in Fig. 7(a)] are shown in Fig. B1. It can be seen that the designed pillar heights with precisions of Pr = 0.5 and 1.0 mm have a satisfactory focusing effect like that of Pr = 0.1 mm. This indicates that the focusing PEMC has good robustness. It should be pointed out that when the total width of the metasurface is constant, the focal distance can be arbitrarily designed in the range of more than half wavelength. The smaller the designed focal distance is, the smaller the error between simulated focal distance and theoretical one is, and vice versa [52, 53].

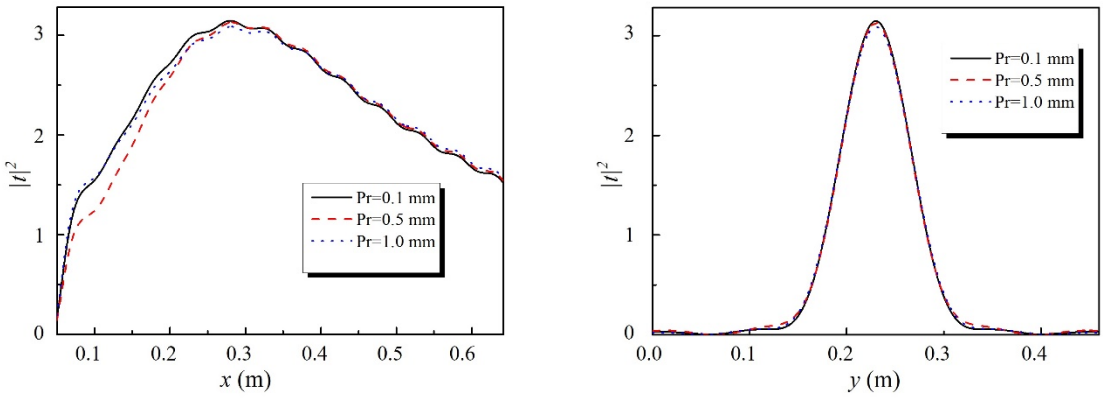

Fig. B1. The focusing results at the frequency of 1 kHz with a focal distance of 3λ with different precision. (a) and (b) the corresponding intensity at the focal spot along the transverse and longitudinal directions.

Appendix C: The PEMC for splitting flexural waves

The PEMC capable of splitting flexural waves can also be designed. This design can split the incident flexural wave beam into two same beams at the same time, which can ensure the integrity of the original plate without introducing any damage. The model of the PEMC is based on the above designed subunits. It consists of the two symmetrical supercells and is illustrated in the upper left corner of Fig. C1(a). In the model, there is only constructive interference without destructive one. The spatial phase shift gradient of the two supercells are $d\phi/dy=2\pi/(12w_1)$ and $d\phi/dy=-2\pi/(12w_1)$. The theoretical refraction angles of $\pm 31.0^{o}$ are superimposed on the full wave fields in Fig. C1(a). The theoretical refraction angles have an excellent agreement with the numerical ones $\pm 27.5^{o}$ from the polar directivity graphs of the transmitted waves in Fig. C1(b). It confirms that the PEMC has effective splitting functionality for flexural waves.

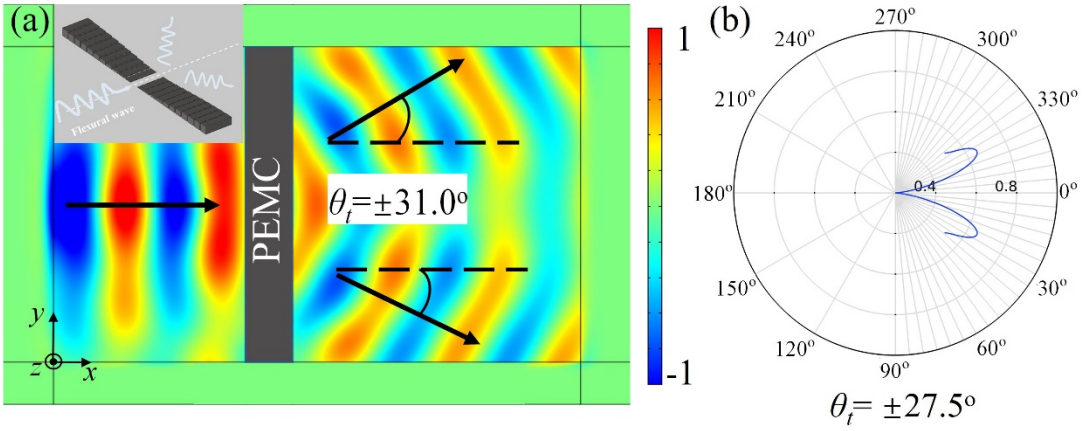

Fig. C1. (a) shows spitting the incident flexural wave by the PEMC. The model of the PEMC, which consists of the two symmetrical supercells, is illustrated in the upper left corner. (b) illustrates the polar directivity graph of the transmitted wave measured at two wavelengths away from the center of the PEMC.

References

[1] Z.Y. Liu, X.X. Zhang, Y.W. Mao, Y.Y. Zhu, Z.Y. Yang, C.T. Chan, P. Sheng, Locally resonant sonic materials, Science, 289 (2000) 1734-1736.

[2] R. Zhu, X.N. Liu, G.K. Hu, C.T. Sun, G.L. Huang, Negative refraction of elastic waves at the deep-subwavelength scale in a single-phase metamaterial, Nat. Commun., 5 (2014) 5510.

[3] G. Hu, L. Tang, X. Cui, On the modelling of membrane-coupled Helmholtz resonator and its application in acoustic metamaterial system, Mech Syst Signal Pr, 132 (2019) 595-608.

[4] R. Zhu, Y.Y. Chen, M.V. Barnhart, G.K. Hu, C.T. Sun, G.L. Huang, Experimental study of an adaptive elastic metamaterial controlled by electric circuits, Appl Phys Lett, 108 (2016) 011905.

[5] R. Zhu, H. Yasuda, G.L. Huang, J.K. Yang, Kirigami-based Elastic Metamaterials with Anisotropic Mass Density for Subwavelength Flexural wave Control, Sci. Rep., 8 (2018) 483.

[6] Lea Sirota, F. Semperlotti, A.M. Annaswamy, Tunable and reconfigurable mechanical transmission-line metamaterials via direct active feedback control, Mech Syst Signal Pr, 123 (2019) 117-130.

[7] C.W. Zhou, J.P. Lainé, M.N. Ichchou, A.M. Zine, Numerical and experimental investigation on broadband wave propagation features in perforated plates, Mech Syst Signal Pr, 75 (2016) 556-575.

[8] P. Li, S. Biwa, The SH0 wave manipulation in graded stubbed plates and its application to wave focusing and frequency separation, Smart Materials and Structures, 28 (2019) 115004.

[9] N.F. Yu, P. Genevet, M.A. Kats, F. Aieta, J.P. Tetienne, F. Capasso, Z. Gaburro, Light Propagation with Phase Discontinuities: Generalized Laws of Reflection and Refraction, Science, 334 (2011) 333-337.

[10] A.V. Kildishev, A. Boltasseva, V.M. Shalaev, Planar Photonics with Metasurfaces, Science, 339 (2013) 1232009.

[11] N.F. Yu, F. Capasso, Flat optics with designer metasurfaces, Nature materials, 13 (2014) 139-150.

[12] B. Assouar, B. Liang, Y. Wu, Y. Li, J. Cheng, Y. Jing, Acoustic metasurfaces, Nat. Rev. Mater., 3 (2018) 460-472.

[13] Y. Li, C. Shen, Y. Xie, J. Li, W. Wang, S.A. Cummer, Y. Jing, Tunable asymmetric transmission via Lossy acoustic metasurfaces, Phys Rev Lett, 119 (2017).

[14] Y. Zhu, J. Hu, X. Fan, J. Yang, B. Liang, X. Zhu, J. Cheng, Fine manipulation of sound via lossy metamaterials with independent and arbitrary reflection amplitude and phase, Nat. Commun., 9 (2018)

1632.

[15] S.W. Fan, S.D. Zhao, A.L. Chen, Y.F. Wang, B. Assouar, Y.S. Wang, Tunable Broadband Reflective Acoustic Metasurface, Phys. Rev. Applied, 11 (2019) 044038.

[16] X.S. Su, Z.C. Lu, A.N. Norris, Elastic metasurfaces for splitting SV- and P-waves in elastic solids, J Appl Phys, 123 (2018) 091701.

[17] L.Y. Cao, Z.C. Yang, Y.L. Xu, Steering elastic SH waves in an anomalous way by metasurface, J. Sound Vib., 418 (2018) 1-14.

[18] Y.L. Xu, Y. Li, L.Y. Cao, Z.C. Yang, X.L. Zhou, Steering of SH wave propagation in electrorheological elastomer with a structured meta-slab by tunable phase discontinuities, Aip Adv, 7 (2017) 095114.

[19] J.Z. Longhai Zenga, b,*, Y.L. T , Youxuan Zhaoa, Ning Hu, Asymmetric transmission of elastic shear vertical waves in solids, Ultrasonics, (2019).

[20] X.H. Shen, C.T. Sun, M.V. Barnhart, G.L. Huang, Elastic wave manipulation by using a phase-controlling meta-layer, J Appl Phys, 123 (2018).

[21] Y.L. Xu, Z.C. Yang, L.Y. Cao, Deflecting Rayleigh surface acoustic wave by meta-ridge with gradient phase shift, J. Phys. D Appl. Phys., 51 (2018) 175106.

[22] H. Zhu, F. Semperlotti, Anomalous Refraction of Acoustic Guided Waves in Solids with Geometrically Tapered Metasurfaces, Phys Rev Lett, 117 (2016) 034302.

[23] Y.Q. Liu, Z.X. Liang, F. Liu, O. Diba, A. Lamb, J.S. Li, Source Illusion Devices for Flexural Lamb Waves Using Elastic Metasurfaces, Phys Rev Lett, 119 (2017) 034301.

[24] H. Lee, J.K. Lee, H.M. Seung, Y.Y. Kim, Mass-stiffness substructuring of an elastic metasurface for full transmission beam steering, J. Mech. Phys. Solids, 112 (2018) 577-593.

[25] J. Zhang, X. Su, Y.L. Liu, Y.X. Zhao, X. Jing, N. Hu, Metasurface constituted by thin composite beams to steer flexural waves in thin plates, Int. J. Solids Struct., 162 (2018) 14-20.

[26] Z. Tian, L. Yu, Elastic Phased Diffraction Gratings for Manipulation of Ultrasonic Guided Waves in Solids, Phys. Rev. Appl., 11 (2019) 024052.

[27] W. Xu, M. Zhang, J. Ning, W. Wang, T. Yang, Anomalous refraction control of mode-converted elastic wave using compact notch-structured metasurface, Mater. Res. Express, 6 (2019) 065802.

[28] Y.L. Xu, L.Y. Cao, Z.C. Yang, Deflecting incident flexural waves by nonresonant single-phase meta-

slab with subunits of graded thicknesses, J Sound Vib, 454 (2019) 51-62.
[29] M.Lott, P. Roux, Effective impedance of a locally resonant metasurface, Phys. Rev. Materials, 3 (2019) 065202.
[30] H. Qiu, M. Chen, Q. Huan, F. Li, Steering and focusing of fundamental shear horizontal guided waves in plates by using multiple-strip metasurfaces, EPL (Europhysics Letters), 127 (2019) 46004.
[31] J. Park, D. Lee, J. Rho, Recent Advances in Non-Traditional Elastic Wave Manipulation by Macroscopic Artificial Structures, Applied Sciences, 10 (2020).
[32] L. Cao, Z. Yang, Y. Xu, S.-W. Fan, Y. Zhu, Z. Chen, B. Vincent, B. Assouar, Disordered Elastic Metasurfaces, Phys. Rev. Appl., 13 (2020) 014054.
[33] L.Y. Cao, Z.C. Yang, Y.L. Xu, B.M. Assouar, Deflecting flexural wave with high transmission by using pillared elastic metasurface, Smart Mater Struct, 27 (2018) 075051.
[34] V. Giurgiutiu, Structural Health Monitoring with Piezoelectric Wafer Active Sensors, Academic Press, London, UK, (2007).
[35] S.L. Li, J.W. Xu, J. Tang, Tunable modulation of refracted lamb wave front facilitated by adaptive elastic metasurfaces, Appl Phys Lett, 112 (2018) 021903.
[36] Y.Y. Chen, X.P. Li, H. Nassar, G.K. Hu, G.L. Huang, A programmable metasurface for real time control of broadband elastic rays, Smart Mater Struct, 27 (2018) 115011.
[37] S.M. Yuan, A.L. Chen, Y.S. Wang, Switchable multifunctional fish-bone elastic metasurface for transmitted plate wave modulation, J Sound Vib, 470 (2020) 115168.
[38] R. Xia, J. Yi, Z. Chen, Z. Li, In situ steering of shear horizontal waves in a plate by a tunable electromechanical resonant elastic metasurface, Journal of Physics D: Applied Physics, 53 (2019) 095302.
[39] M.S. Kim, W.R. Lee, Y.Y. Kim, J.H. Oh, Transmodal elastic metasurface for broad angle total mode conversion, Appl Phys Lett, 112 (2018) 241905.
[40] Y. Xu, L. Cao, P. Peng, X. Zhou, B. Assouar, Z. Yang, Beam splitting of flexural waves with a coding meta-slab, Appl Phys Express, 12 (2019) 097002.
[41] L.Y. Cao, Y.L. Xu, B. Assouar, Z.C. Yang, Asymmetric flexural wave transmission based on dual-layer elastic gradient, Appl Phys Lett, 113 (2018) 183506.
[42] H.F. Zhu, T.F. Walsh, F. Semperlotti, Total-internal-reflection elastic metasurfaces: design and

application to structural vibration isolation, Appl Phys Lett, 113, (2018) 221903.
[43] Y.B. Jin, E. El Boudouti, Y. Pennec, B. Djafari-Rouhani, Tunable Fano resonances of Lamb modes in a pillared metasurface, J Phys D Appl Phys, 50 (2017) 425304.
[44] U. Fano, Effects of configuration interaction on intensities and phase shifts, Phys. Rev. , 124 (1961) 1866.
[45] C. Goffaux, J. SánchezDehesa, A.L. Yeyati, P. Lambin, A. Khelif, J. Vasseur, B. DjafariRouhani, Evidence of Fano-Like interference phenomena in locally resonant materials, Phys Rev Lett, 88 (2002) 225502.
[46] Y.A. Kosevich, C. Goffaux, J. SánchezDehesa, Fano-like resonance phenomena by flexural shell modes in sound transmission through two-dimensional periodic arrays of thin-walled hollow cylinders, Phys Rev B, 74 (2006) 012301.
[47] J.D. Achenbach, Wave Propagation in Elastic Solids, (Amsterdam: North-Holland), pp (1973) 254–256.
[48] F.L. Degertekin, B.T. Khuri-Yakub, Single mode Lamb wave excitation in thin plates by Hertzian contacts Appl Phys Lett, 69 (1996) 146.
[49] F.J. Fahy, P. Gardonio, Sound and Structural Vibration: Radiation, Transmission and Response (Academic Press), (2007).
[50] K.F. Graff, Wave motion in elastic solids, Oxford University Press, Oxford, UK., (1975).
[51] P.E. Cho, Energy flow analysis of coupled structures, Ph.D. Thesis, Purdue University, West Lafayette, IN, (1993).
[52] S. Zhang, L. Yin, N. Fang, Focusing Ultrasound with an Acoustic Metamaterial Network, Phys Rev Lett, 102 (2009) 194301.
[53] S.D. Zhao, A.L. Chen, Y.S. Wang, C.Z. Zhang, Continuously Tunable Acoustic Metasurface for Transmitted Wavefront Modulation, Phys. Rev. Applied, 10 (2018) 054066.